Title

Observations and parameterization of the effects of barrier height and source-to-barrier distance on concentrations downwind of a roadway

Journal

Atmospheric Pollution Research, 13(4)

ISSN

1309-1042

Authors

Francisco, Dianna M
Heist, David K
Venkatram, Akula
et al.

Publication Date

2022-04-01

DOI

10.1016/j.apr.2022.101385

Peer reviewed

Published in final edited form as:
Atmos Pollut Res. 2022 March 16; 13(4): 1–101385. doi:10.1016/j.apr.2022.101385.

Observations and Parameterization of the Effects of Barrier Height and Source-to-Barrier Distance on Concentrations Downwind of a Roadway

Dianna M. Francisco[1], **David K. Heist**[2], **Akula Venkatram**[3], **Lydia H. Brouwer**[4], **Steven G. Perry**[2]

[1]ORAU ORISE Research Participation Program hosted at U.S. EPA, Research Triangle Park, NC, USA

[2]U.S. EPA ORD/CEMM, 109 T.W. Alexander Dr., MD 81, Research Triangle Park, NC, USA

[3]University of California-Riverside, Riverside, CA, USA

[4]Jacobs Technology, Inc., Research Triangle Park, NC, USA

Abstract

New results are presented from wind tunnel studies performed at the United States Environmental Protection Agency (U.S. EPA), which include cases with solid roadside barriers of varying heights and cases with varying distances between the line source (roadway) and a 6-m-tall barrier. The *Source-to-Barrier Distance* cases include seven lanes of traffic with each lane acting as an independent source of continuous emissions along a line (i.e., line source). A mixed-wake algorithm that accounts for barrier effects within a steady-state air dispersion model was updated based on the recent wind tunnel studies. To study the effects of a solid roadside barrier, varying barrier heights and varying distances between the line source and barrier were modeled with the U.S. EPA regulatory air dispersion model AERMOD (v. 21112) using the line-source option that includes an experimental barrier option (RLINEXT). The mixed-wake algorithm reproduced the shape of the vertical concentration profiles observed in the wind tunnel data, including the uniform concentration profile from the ground vertically to a height somewhat greater than the height of the barrier. The algorithm responded appropriately to changes in barrier height and source-to-barrier distance, producing greater reductions in ground-level concentrations for taller barriers and for shorter source-to-barrier distances. Additionally, a rule of thumb that approximates the effect of a downwind barrier was formulated by converting an estimated vertical dispersion into an additional travel distance. The wind tunnel results, the update to the mixed-wake algorithm, and a comparison of the two data sets are described in this paper.

[6]**Publisher's Disclaimer:** Disclaimer
The U.S. Environmental Protection Agency, through its Office of Research and Development, funded and directed the research described herein. It has been subjected to the Agency's review and has been approved for publication. Note that approval does not signify that the contents necessarily reflect the views of the Agency. Mention of trade names, products, or services does not convey official U.S. EPA approval, endorsement, or recommendation. This project was supported in part by an appointment to the Research Participation Program at the ORD/CEMM, U.S. EPA, administered by the Oak Ridge Institute for Science and Education through an interagency agreement between the U.S. Department of Energy and U.S. EPA.

Keywords

mobile sources; wind tunnel; AERMOD; dispersion modeling; solid barrier

1. Introduction

Numerous air quality monitoring studies have identified a wide range of adverse health effects experienced by people exposed to traffic-related air pollution (TRAP) at varying distances from a roadway. These health effects include increased risk of respiratory illness, cancer, birth and developmental effects, and premature mortality (Jerrett et al., 2009; HEI, 2010). Adverse health effects of TRAP range from short-term effects such as altering a person's blood pressure, heart rate, and heart rate variability, to long-term effects such as an enhanced risk of cardiovascular disease (Han et al., 2021). TRAP consists of a complex mixture of various pollutants (e.g., carbon monoxide, nitrogen oxides, hydrocarbons, particulate matter) that disperse downwind of a roadway by local winds.

Numerous studies over the past decade have demonstrated the importance of the roadway geometry or source configuration on dispersion of pollutants from mobile sources. These roadway configurations include street canyons, roadside vegetation, depressed roadways, solid noise barriers, and elevated highways configured as viaducts, among others (e.g., Heist et al., 2009; Amini et al., 2018; Joerger and Pryor, 2018; Hao et al., 2019). Some of these configurations such as trees within a street canyon have been shown to increase concentrations within the canyon or downwind of the roadway (e.g., Gromke and Ruck, 2012; Yang et al., 2020). Others, such as depressed roadways and roadside noise barriers have the potential to significantly reduce downwind concentrations relative to that for a roadway in flat terrain and no barriers. Also, a single roadway configuration can give rise to both elevated concentrations at some locations and lower concentrations at different locations. People spend about 90% of their time inside buildings of various heights, which raises the importance of studying how noise barriers affect the vertical distributions of concentrations (Zhang et al., 2019). These various studies have shown that roadway configuration can have a considerable effect on dispersion of roadway emissions.

Solid noise barriers have been the subject of numerous studies, including wind tunnel measurements (Heist et al., 2009), computational fluid dynamic simulations (Hagler et al., 2011; Wang and Wang, 2021) and in field experiments (Finn et al., 2010). As is the case with other roadway configurations, the specifics of the configuration – whether the barrier is upwind or downwind of a roadway, the height of the barrier, or the distance between the roadway and the barrier – influence the impact of the barrier on downwind dispersion. Another common configuration has barriers on both sides of the roadway, which has been examined by Ahangar et al. (2017).

This paper, focused on roadside barriers on the downwind side of the roadway, has two major parts. The first presents new results from wind tunnel observations that examine the effects on near-road concentrations due to solid roadside barriers of varying heights (i.e., full-scale equivalent heights of 3 m, 4.5 m, 6 m, and 9 m), and of varying distances between the line source and a 6-m-tall barrier (full-scale equivalent distances of 6 m to 30 m upwind

of the barrier). As far as we are aware, these wind tunnel studies performed at the United States Environmental Protection Agency (U.S. EPA) are the first experimental results on these particular barrier effects. In the second part of the paper, we use the wind tunnel results to parameterize these effects in the dispersion modeling system, AERMOD (Cimorelli et al., 2005), with a line-source option (Snyder et al., 2013) that includes an experimental barrier option (RLINEXT). This parameterization builds on the mixed-wake algorithm described in Venkatram et al. (2021). Model results are shown using AERMOD (v. 21112), which includes the latest mixed-wake algorithm update described in this paper (U.S. EPA, 2021). Finally, a rule of thumb is discussed that approximates the effect of a downwind barrier on dispersion by converting an estimated vertical dispersion into an additional travel distance.

2. Wind tunnel studies

Two sets of wind tunnel measurements were performed at U.S. EPA's Fluid Modeling Facility (Snyder, 1979) to examine both the effect of the height of a roadside noise barrier and the source-to-barrier distance on the resulting concentrations downwind of a roadway. The experiments were performed in the facility's meteorological wind tunnel.

2.1. Wind tunnel model and cases

The meteorological wind tunnel where the experiments were performed had a cross-section measuring 3.5 m wide and 2.1 m tall with a fetch of 18 m. The wind tunnel setup was designed to simulate a neutrally-stable boundary layer typical of a suburban area where noise barriers are frequently located next to roadways. To produce the scaled atmospheric boundary layer, air from the wind tunnel inlet first flowed past five Irwin spires (Irwin, 1981) followed by an array of square-edged roughness tabs along the floor of the tunnel, which produced and maintained the boundary layer (see Heist and Perry, 2018 and Perry et al., 2016, for more details regarding the wind tunnel and scaled boundary layer specifications). Figs. S1 and S2 show photographs of the interior of the wind tunnel and plots of vertical profiles of wind speed and turbulence quantities, respectively. The tunnel ceiling height was adjusted along the length of the tunnel to account for the small flow blockage created by the model (approximately 1.9%) and to allow for a non-accelerating free-stream flow. Fitting the velocity and turbulence profiles (measured with laser Doppler velocimetry with a free-stream velocity of 4.7 m/s) produced a full-scale equivalent surface roughness height (z_0) and friction velocity (u_*) of 0.27 m and 0.25 m/s, respectively (Perry et al., 2016), and the measured turbulence profiles were in good agreement with profiles typically observed in the surface layer of an atmospheric boundary layer. The boundary layer depth was estimated to be approximately 200 m, full-scale. The Reynolds number (Re) for this study (based on nominal barrier height of 6 m and a reference wind speed of 2.98 m/s) was approximately 8,000, somewhat less than the recommended value of 11,000 for the flow to be independent of Re (Snyder, 1981). To address this concern, concentration measurements were repeated for a subset of the cases at a 50% higher reference wind speed, and concentration profiles (normalized as described below with the corresponding reference wind speed) were nearly identical to the results at the lower wind speed indicated that Reynolds number independence was achieved.

The roadway source was simulated by three roadway segments lined up end to end to represent a single line source. Each roadway segment simulated in the wind tunnel was 91 cm long, resulting in the full-scale equivalent dimensions of 136.5 m long with a model scale of 1:150 (Figs. 1a and 1b). A single line source represented a single lane of traffic with a length of 409.5 m (full scale). Each line-source segment in the model was constructed of a 91-cm-long, thin-walled, hollow, square (0.6 cm outside dimension) brass tube. Holes were drilled roughly 0.1 cm in diameter and spaced 1 cm apart along the center of the downward face of all tubes, which provided emission ports for the uniform release of the tracer gas (Figs. 1c and 1d). Tabs were mounted on the upwind side of the tubes, directly upwind of each emission port, to promote mixing. The tabs were 0.3 cm wide and protruded 0.5 cm below the source tube. The resulting emissions entered the wind tunnel at a full-scale height of 1.5 m (Fig. 1c) and were mixed by both the tabs and the wake of the source tube to simulate the effect of mixing in the wakes of vehicles. The tracer gas was metered through mass flow controllers and was a mixture of high-purity ethane (C_2H_6; Chemically Pure grade; minimum purity 99.5 mole percent) and air. Ethane was chosen because its molecular weight (30.07 g/mol) is nearly equivalent to that of dry air (28.97 g/mol) and this mixture provided a near neutrally buoyant tracer gas. For the one-source cases, the mass flow rate of ethane was set at 1.875 g/min and air was set at 5.4 g/min. For the two-source cases, the mass flow rate of ethane was held at 1.875 g/min and air was delivered at 12.6 g/min (resulting in a total flow rate roughly twice the one-source rate).

Two sets of cases were studied in the wind tunnel: *Barrier Height* cases examined the effect of barrier height and *Source-to-Barrier Distance* cases examined the effect of the separation distance between the lane of traffic and the downwind barrier. These experiments used a continuous release from either a single line source or two parallel line sources, and a solid barrier located on the downwind side of the line source(s). For comparison with the barrier cases, a no-barrier configuration was also measured for each setup (*No Barrier* cases). The barrier was constructed from a vertical steel plate (0.1 cm thick) and was oriented parallel to the line source(s). Winds flowed perpendicular to the line source(s) and barrier. The origin of the coordinate system was located on the tunnel floor at the center of the barrier, with positive x in the streamwise direction, y along the barrier, and z vertically upward (Fig. 1).

For cases examining the effect of barrier height (i.e., *Barrier Height cases)*, two line sources were fixed in location at full-scale equivalent locations of −27.9 m and −8.1 m with the center of those two lanes at −18 m (Fig. 1a). The barrier height, denoted as h_b, varied (i.e., based on the full-scale equivalent of 3 m, 4.5 m, 6 m, and 9 m). The range of heights studied covers the range in a recent inventory of noise barriers available from the U.S. Federal Highway Administration (FHWA, 2021). For the cases examining the effect of source-to-barrier distance (i.e., *Source-to-Barrier Distance* cases), a line source was located at various upwind distances (i.e., full-scale equivalent of 6 m, 10 m, 14 m, 18 m, 22 m, 26 m, and 30 m) from the barrier, denoted as d_b (Fig. 1b). The barrier height was 6 m (full scale) for these cases, chosen to represent the average height from range of heights used in the *Barrier Height* cases.

H is denoted as the length scale used to normalize distances and lengths throughout this paper, representing a nominal barrier height of 6 m. Note that this is distinct from the barrier

height, h_b, which ranges from 3 m to 9 m (or 0 m for the *No Barrier* cases). Therefore, the line source(s) and the barrier were each 68.25H long.

2.2. Wind tunnel measurement methods

Tracer samples were collected through 0.24-cm outside-diameter brass tubes arranged in groups of six on vertical and horizontal sampling rakes to measure vertical and longitudinal concentration profiles. All samples were drawn through Rosemount Model 400A hydrocarbon analyzers (flame ionization detectors) operating in the continuous sampling mode (for a continuous tracer release). The output signals from the analyzers were acquired at the rate of 20 Hz averaged over 120 s. The hydrocarbon analyzers were calibrated daily against a range of certified standardized gases. The background concentration of the tracer gas was monitored over the measurement period and was subtracted from the sample concentration. The concentration measurements are reproducible within ±5% at the center of the plume and within ±10% at the plume edges where variability in concentration is higher.

Concentrations were measured at various heights, from $z/H = 0$ to $z/H = 6$ (with a vertical spacing of 0.75 m full scale), and at nine locations along x (at $y = 0$). The vertical profiles were measured downwind of the barrier at $x/H = 0.125$, 1, 2, 4, 7, 12, 17, 27, and 37. Measured concentrations were normalized as:

$$\chi = CU_r L_x / (Q / L_y) \quad (1)$$

where C is the measured concentration (g/m^3), U_r is the reference wind speed (2.98 m/s) at the reference height (20 cm, 30 m full scale), L_x is the nominal along-wind dimension of the roadway segment (24 cm, 36 m full scale), L_y is the cross-wind length of the roadway (273 cm, 409.5 m full scale), and Q is the tracer emission rate (1.875 g/min).

2.3. Wind tunnel results

To examine the effects of barrier height on pollutant concentrations downwind of a roadway, vertical profiles of non-dimensional concentration are plotted in Fig. 2 for barrier heights ranging from 0 m (i.e., *No Barrier*) to 9 m at four downwind distances. The *No Barrier* case shows a peak in concentrations within the typical breathing level of $z/H = 0$ to $z/H = 0.33$, and then a rapid decrease in concentration with increasing height. With a barrier present, the concentration plume shape downwind of the barrier is relatively constant with height from ground level to just beyond the top of the barrier, and then concentrations rise to a peak above the barrier before decreasing with height. This plume shape is consistent with the vertical profile used for the mixed-wake model (Schulte et al., 2014; Venkatram et al., 2021) described in section 3. As barrier height increases, concentrations are lower at ground level, which indicates that a taller barrier is more effective at lowering concentrations downwind of the barrier.

The maximum breathing-level concentrations for *Barrier Height* cases occur immediately downwind of the barrier ($x/H = 0.125$) and then decrease with downwind distance (Fig. 3a). The *No Barrier* case shows a large gradient in concentration with downwind distance compared to the *Barrier* cases due to higher starting values at the edge of the roadway ($x/H =$

0). The *No Barrier* case breathing-level concentrations decrease by approximately 60% from the edge of the road to $x/H = 7$ downwind. For the tallest barrier (9 m), the breathing-level concentrations are more uniform between the barrier location and $x/H = 7$ with a reduction of 15% over this distance. Breathing-level concentrations decrease with increasing barrier height, which illustrates how an increase in barrier height leads to increased vertical mixing and hence a greater decrease in concentrations downwind of the roadway relative to those in absence of a barrier. For example, at $x/H = 0.125$ average breathing-level concentrations for the *Barrier* cases are reduced by roughly 31%, 49%, 52%, and 71% relative to the *No Barrier* case for barrier heights of 3 m, 4.5 m, 6 m, and 9 m, respectively. This shows that even a short barrier contributes to lower downwind concentrations, primarily close to the barrier.

With respect to the *Source-to-Barrier Distance* cases, the maximum breathing-level concentrations occur immediately downwind of the barrier, and then decrease with downwind distance (Fig. 3b). Breathing-level concentrations decrease with increasing source-to-barrier distance, but there is less variation in concentrations between *Source-to-Barrier Distance* cases compared to the *Barrier Height* cases shown in Fig. 3a. This illustrates that moving the roadway (line source) farther upwind of the barrier can slightly lower breathing-level concentrations downwind of the barrier. For example, at $x/H = 0.125$ average breathing-level concentrations for the *Barrier* cases are reduced by roughly 10%, 8%, 13%, 16%, 20%, and 34% relative to the 6-m distance case for source-to-barrier distances of 10 m, 14 m, 18 m, 22 m, 26 m, and 30 m, respectively. Although not shown in the figure, the reduction in breathing-level concentrations immediately downwind of the barrier (compared to *No Barrier*) is approximately 50% for most lanes of traffic, but it can be reduced by as much as 60% for lanes closest to the barrier.

Fig. 4 shows the velocity and turbulence fields, using the tallest barrier height (9 m) case as an example, to illustrate the effect of a solid barrier on these fields. As the approach flow is pushed over the barrier, higher wind speeds are observed in the area above the recirculation region. The resulting high wind shear generates elevated levels of turbulence downwind of the barrier with a maximum located at approximately $x/H = 9$ at a height of approximately $z/H = 2$. This elevated level of turbulence will enhance the rate at which the plume disperses vertically. Wind in the wake of the barrier is slower than the incoming flow and changes direction as a result of the recirculation zone just downwind of the barrier. The portion of the plume that is entrained into the recirculation region will therefore advect downwind with a slower wind speed than the portion of the plume that remains aloft. The recirculation zone extends from the barrier to a location between $x/H = 6$ and $x/H = 12$ for this 9-m barrier case.

Observations in the concentration and wind velocity fields from the wind tunnel experiments will be used in the next section to formulate updates to the mixed-wake algorithm. In particular, the mixed-wake algorithm will include lofting of the plume over the barrier, a well-mixed concentration field downwind of and below the barrier height, and elevated turbulence downwind of the barrier that leads to increased vertical plume spread.

3. Mixed-wake algorithm

Schulte et al. (2014) introduced the idea of a mixed-wake algorithm to represent the concentration patterns observed downwind of a noise barrier. Specifically, the algorithm assumed that the concentration was well-mixed from the ground level to the height of the barrier within the recirculation region and followed a Gaussian shape above the barrier. These two parts of the plume were advected by wind speed representative of each region: one wind speed (U_w) for the well-mixed region and an effective wind speed at mean plume height (U_{eff}) for the upper region. Further refinements to this initial algorithm were added by Ahangar et al. (2017) and Venkatram et al. (2021), including a reflection term for the Gaussian portion of the profile and a scaling factor to maintain mass balance.

The formulation of the model is based on a two-step modification of the emitted plume by the barrier. Upwind of the barrier, the plume disperses as it would in the absence of the barrier; the concentration profile accounts for reflection at the ground. At the barrier location, the entire plume is lifted by an amount z_h, and then partially entrained into the wake of the barrier as it is carried downwind by the wind. In Venkatram et al. (2021), z_h is taken to be the barrier height, h_b. Observations from the wind tunnel results indicate that the plume lofts by an amount greater than h_b as it moves over the barrier, suggesting an increase in this parameter to $z_h = 1.25h_b$ to better represent the vertical extent of the well-mixed region downwind of the barrier (see Fig. 2). The concentration below z_h is well mixed, and the concentration profile above this height is Gaussian with an adjustment factor f_q to maintain constancy of horizontal flux of material. The details of the formulation follow.

In the mixed-wake algorithm, the concentration profile, $C(z)$, is described as:

$$C = C_s \qquad z < z_h \quad (2)$$

$$C = f_q \frac{1}{\sqrt{2\pi}\sigma_z U_{eff}} \left[exp\left(-\frac{1}{2}\left(\frac{z - (z_h + z_{src})}{\sigma_z} \right)^2 \right) + exp\left(-\frac{1}{2}\left(\frac{z - (z_h - z_{src})}{\sigma_z} \right)^2 \right) \right] \qquad z > z_h \quad (3)$$

where C_s is the concentration in the well-mixed region, f_q is a scaling factor, σ_z is the vertical dispersion coefficient, U_{eff} is the effective wind speed above z_h, z_{src} is the original source height, and z is the receptor height (see Fig. 5a). The plume is lofted over the barrier and is assumed to be released at an effective source height of $z_h + z_{src}$ (with a reflection at $z_h - z_{src}$) as shown in Fig. 5b.

To find the scaling factor f_q, we first ensure that the concentration profile described in Equation (3) is continuous at $z = z_h$, i.e.,

$$C(x, z = z_h) = C_s = f_q \frac{2}{\sqrt{2\pi}\sigma_z U_{eff}} exp\left[\left(-\frac{1}{2}\left(\frac{z_{src}}{\sigma_z} \right)^2 \right) \right] \quad (4)$$

and that the horizontal flux is equal to the source strength q_y. Integrating the plume through its depth gives:

$$q_y = \int_0^{z_h} U_w C_s \, dz + \int_{z_h}^{\infty} U_{eff} \, C \, dz \tag{5}$$

where U_w is the advection velocity for the lower part of the plume and q_y is the emission rate of the line source per unit length. Casting Equation (4) as $C_s = f_q C_q$ and solving Equations (4) and (5) for f_q yields:

$$f_q = \frac{q_y}{1 + (U_w C_q z_h)} \tag{6}$$

The two wind speeds used in Equation (5), U_w (below z_h) and U_{eff} (above z_h), are chosen to represent the two different parts of the plume (Fig. 5a). U_w is nominally taken to be half the wind speed at barrier height, but with an additional factor included to account for lower winds seen close to the barrier. This factor, f_{Uw}, is formulated to be smallest near the barrier and approach unity with downwind distance:

$$U_w = 0.5 f_{Uw} U_{hb} \tag{7}$$

$$f_{Uw} = 1 - A \, exp(-\frac{x_d}{9h_b}) \tag{8}$$

where x_d is the downwind distance from the barrier to the receptor, and U_{hb} is the wind speed at barrier height. The rate at which the factor f_{Uw} approaches unity is determined by the scale $9h_b$, which is roughly the horizontal extent of the recirculating region behind the barrier. The data indicated that the factor A in Equation (8) decreased with barrier height, and the empirical fit to the data turned out to be $A = \left(1 - \frac{0.75 h_b}{h_{max}}\right)$, where h_{max} is either the barrier height or 12 m, whichever is greater. Barriers taller than 12 m are rare, and lacking data to draw on, no further decrease in U_w is made for barriers above that limit.

U_{eff} is calculated at the height of the center of mass of that portion of the plume above z_h based on the approach of AERMOD's RLINE source type (Snyder et al., 2013; Venkatram et al., 2013). The velocity profile used in the estimate of U_{eff} is calculated using Monin-Obukhov similarity theory with a friction velocity (u_*) value that reflects the elevated turbulence levels observed near the barrier. Specifically, the value of u_* is enhanced by a factor $\alpha = (z_{0,\,barrier}/z_0)^{0.14}$, where $z_{0,barrier}$ is the roughness downwind of the barrier taken to be $H/9$ (Venkatram and Schulte, 2018). The u_* enhancement, which affects the boundary layer downwind of the barrier, leads to an increase in the magnitude of the Obukhov length and displacement height.

Finally, the effect of the barrier on the vertical spread of the plume is considered. Upwind of the barrier, the plume spreads according to the formulations in Venkatram et al. (2013), which have no barrier effects. Since vertical plume spread (σ_z) is a function of u_*, the plume initially grows with the ambient value of u_* until the plume reaches the barrier.

Upon encountering the barrier, the plume is further mixed by interaction with this obstacle. To account for this mixing and assuming the additional vertical mixing is proportional to the barrier height, an additional $0.1H$ is added to the vertical plume spread, which is then recharacterized as an "initial" σ_z value for calculations downwind of the barrier. Downwind of the barrier, the plume grows at an enhanced rate proportional to the new value of u_* described above.

4. Results and discussion

The mixed-wake algorithm described above has been implemented in AERMOD (v. 21112), a steady-state plume model that incorporates air dispersion formulated from atmospheric boundary layer physics for both surface and elevated sources (U.S. EPA, 2021). AERMOD contains numerous source types, including RLINE and RLINEXT, which are designed to model the dispersion of line source emissions in neutrally-stable atmospheric conditions using the Monin–Obukhov similarity theory to vertically scale the winds and turbulence (Cimorelli et al., 2005; Perry et al., 2005). The line-source type RLINE is based on a Gaussian plume and is designed to simulate vehicle emissions by integrating point sources along a line source to compute concentrations. RLINEXT, an extension of the RLINE source type with additional features still under development, includes the mixed-wake algorithm described above for modeling barriers downwind of a roadway. The RLINEXT source type was used to simulate the noise barrier cases described in section 2. Details on the model setup can be found in the Appendix.

4.1 Effect of barrier height

Vertical profiles of concentrations from AERMOD simulations are shown in Fig. 6 against measurements from the wind tunnel for a range of barrier heights and downwind distances. The focus is on downwind distances up to $7H$ since the effects of the barrier are most pronounced in this region. As observed in the wind tunnel data, the mixed-wake algorithm produces a uniform profile below the barrier height, and, in agreement with the data, these near-ground concentrations decrease with increasing barrier height.

Two model simulations were performed to show the improvement afforded by the extra lofting of the plume and the reduction of the wind speed in the wake of the barrier (Fig. 6). The solid black curves represent the algorithm as described in Section 3 while the dashed purple curves represent the previous algorithm that omits the extra lofting of the plume to $1.25h_b$ and the reduction of the wind speed for the portion of the plume in the recirculation region (see equation 8 above). The inclusion of these effects improves the model results; The purple curves clearly show an underprediction of the observed concentrations near the ground for barrier heights 6 m and below and underestimate the degree of vertical lofting of the plume. The model improvement is shown in the black curves, though some underprediction for lower barrier heights (3 m and 4.5 m) remains and is perhaps a result of the parameterization of U_w remaining to overestimate wind speed for those cases. Above the barrier, the concentrations generally decrease with height from the top of the barrier. Above the top of the barrier, the taller barrier cases (6 m and 9 m) show underprediction compared to the wind tunnel. One aspect of these profiles that is not well captured by the model is the

initial rise in concentration above the barrier seen in the wind tunnel data at $x/H = 0.125$. At $x/H = 1$ and beyond, the shape of the vertical profile is well represented by the model.

Model performance was measured using the geometric mean (MG) and the geometric standard deviation (SG), as defined by Venkatram (2008), and the fraction of model estimates (C_p) within a factor of two of the wind tunnel measurements (C_0), denoted as FAC2. Specifically, FAC2 is defined as the proportion of model concentrations that satisfy $0.5 \leq C_p/C_o \leq 2.0$, with an ideal value of 1.0. For both MG and SG, the optimum value is also 1.0.

Fig. 7a shows scatter plots of wind tunnel measured vs. modeled concentrations for the *Barrier Height* cases, where locations closer to the ground ($z/H \leq 1$) are shown in red. The *No Barrier* case ($h_b = 0$) shows the highest concentrations of all cases, and modeled results are tightly clustered around the 1:1 line, indicating good agreement with the observations. In addition, most points are within the factor of two lines yielding a FAC2 value of 0.602 for all points and 1.0 for locations below 6 m. For the *Barrier* cases, the results produced FAC2 values of 0.679, 0.683, 0.704, and 0.736 for barrier heights of 3 m, 4.5 m, 6 m, and 9 m, respectively. For locations below 6 m, the spread is substantially reduced, as reflected by the smaller SG values. In addition, FAC2 equaled the ideal value of 1.0 for all barrier heights. The model tends to underpredict wind tunnel observations, with values of MG that are less than or equal to 1.25 when all points are considered, and less than or equal to 1.2 for $z/H \leq 1$.

Fig. 7b presents the reduction in breathing-level concentrations downwind of a barrier for various heights, shown as the ratio of *Barrier* concentrations to *No Barrier* concentrations. The figure shows both wind tunnel measurements (dots) and model results (smooth lines with shading) within the breathing level. The greatest reduction in concentrations (lowest ratio) is found immediately downwind of the barrier and for the tallest barrier. The reduction in concentration abates with downwind distance but does not reach *No Barrier* concentration levels for barrier heights greater than 3 m. The model captures these general trends observed in the data but sometimes overestimates the amount of reduction in concentrations, especially for the shorter barriers for $x/H \leq 12$.

4.2 Effect of source-to-barrier distance

AERMOD simulations were also performed for the *Source-to-Barrier Distance* cases to examine the response of the model to changes in the distance between a lane of traffic and a downwind noise barrier. Fig. 8 shows vertical profiles of concentration for three source-to-barrier distances representing the shortest, middle, and longest separation distance measured in the wind tunnel. The figure is focused on downwind distances between $x/H = 0.125$ and $x/H = 7$ since the largest effects of the barrier are seen there. The model captures the reduction in concentration observed when a barrier is present, especially in the region between the ground and the top of the barrier. The breathing-level concentrations are sensitive to the source-to-barrier distance when a barrier is present and the barrier effect is greatest for sources closest to the barrier. This effect is well represented by the model (solid line). The elevated peak in concentration above the barrier is found in the model results for the shortest source-to-barrier distance, but the magnitude of the peak is underpredicted and

its height is overpredicted at $x/H = 0.125$. After the elevated peak fades, the shape of the profile predicted by the model consistently reflects the measured shape.

Fig. 9a shows scatter plots of wind tunnel measured vs. modeled concentrations for the *Source-to-Barrier Distance* cases, where locations closer to the ground ($z/H \leq 1$) are shown in red. The *No Barrier* cases (displayed in the left-hand column) show higher concentrations compared to the *Barrier* cases, and modeled results follow the 1:1 line, indicating good agreement with the observations. In addition, most points are within the factor of two lines, yielding a FAC2 value above 0.5. For the *No Barrier* cases, the FAC2 values are 0.544, 0.692, and 0.789 for source-to-barrier distances of 6 m, 18 m, 30 m, respectively. For the *Barrier* cases (right-hand column of Fig. 9a), the results show somewhat higher FAC2 values of 0.726, 0.782, and 0.803 for source-to-barrier distances of 6 m, 18 m, and 30 m, respectively. For heights below 6 m ($z/H \leq 1$), the spread is substantially reduced, as reflected by the smaller SG values and ideal FAC2 values of 1.0 for all cases except the *No Barrier* case with a source-to-barrier distance of 6 m (where FAC2 = 0.944). The model tends to underpredict wind tunnel observations, with values of MG that are less than or equal to 1.1 when all points are considered and less than or equal to 1.18 for $z/H \leq 1$.

Fig. 9b shows the ratio of breathing-level concentrations for the *Source-to-Barrier Distance* cases relative to the *No Barrier* cases measured with sources in the same locations ($\chi_{\text{Barrier}}/\chi_{\text{NoBarrier}}$). As noted above, the greatest reduction in concentration due to a downwind barrier occurs for the lane of traffic closest to the barrier. The concentration ratio does not return to 1.0 within the downwind distance shown (up to $x/H = 37$), which shows the barrier's effect on concentrations continues beyond this distance. Lower values of this ratio indicate a greater effect of the barrier on concentrations. The model predicts somewhat lower concentrations than were observed in the wind tunnel but responds to the source-to-barrier distance appropriately (i.e., greater reduction for lanes closest to the barrier). Fig. 9b also shows that, even for sources 30 m upwind from the barrier, the resulting concentrations are still lower than the *No Barrier* cases.

As a rule of thumb, one can approximate the effect of a noise barrier as an enhancement to the initial dispersion. For the purposes of a rule of thumb, and because atmospheric stability effects will be reduced downwind of the barrier due to enhanced mechanical turbulence (see Fig. 4), one may assume that vertical plume spread (σ_z) grows in proportion to $(u_*/U_{hb})x$ with an initial dispersion equal to the height of the barrier (i.e., $\sigma_z \sim \frac{u_*}{U_{hb}}x + h_b$). The centerline concentration downwind of a barrier can then be written as:

$$C \sim \frac{Q}{U_{hb}\sigma_z} \sim \frac{Q}{U_{hb}\left[\frac{u_*}{U_{hb}}x + h_b\right]} \sim \frac{Q}{U_{hb}\left[\frac{u_*}{U_{hb}}(x + x_0)\right]} \quad (9)$$

where $x_0 = \frac{h_b}{u_*/U_{hb}}$. In other words, the initial dispersion can be recast as an increase in the travel (downwind) distance of the plume, x_0. Since the vertical plume width is directly

proportional to the barrier height, Eq. 9 reveals the inverse relationship between barrier height and concentration.

In Fig. 10, the non-dimensionalized concentrations from Fig. 3a are replotted as a function of $x + x_0$ to test whether this rule of thumb is followed. Beyond roughly 100 m, the concentration curves tend to overlap, except for the 9-m barrier case, which shows somewhat higher concentrations. It may be that for taller barriers, the growth rate of the plume should be enhanced due to the higher levels of turbulence generated. However, as a rule of thumb, one may assume that the effect of a barrier is equivalent to adding an additional travel distance equal to x_0 for distances beyond the immediate wake of the barrier. That is, with knowledge of the *No Barrier* concentration distribution, traveling an extra x_0 downwind will provide rough estimates of the *Barrier* concentrations (from barrier location to downwind). For example, a 6-m barrier would give similar concentrations to a *No Barrier* case with an extra travel distance of 47 m (assuming $u_* = 0.25$ m/s and $U_{hb} = 1.94$ m/s). This rule of thumb offers a useful way to conceptualize the physical effects of a barrier on dispersion downwind from a roadway and may indicate when a more refined analysis is warranted.

4.3 Limitations and future work

As noted in Section 2.1, the Reynolds number is less than the recommended value of 11,000 for *Re* independence. We addressed this concern by repeating a subset of the noise barrier cases at a *Re* that was 50% higher and verified that normalized concentrations were nearly identical to those measured at the lower *Re*. The lower Re achievable in the wind tunnel is a limitation of this approach, and fields studies at full scale are recommended to further evaluate the algorithms.

Because the flow in the wind tunnel is neutrally buoyant and winds are perpendicular to the roadway, there remains a need to examine other atmospheric stabilities and wind directions. Since field experiments have the potential to cover a wide range of conditions including atmospheric stabilities and wind directions, we plan to use observational data from upcoming field research to further evaluate these barrier algorithms. In addition, the wind tunnel studies do not address the effect of thermal buoyancy force (e.g., by wall heating or solar heating) on pollutant dispersion. Further studies are needed to explore those affects.

It is important to note that noise barriers are sometimes positioned on the upwind side of a roadway and can be used on both sides. In addition, barrier heights often vary along their length and have different shapes. Additional work on these cases may be needed to fully capture noise barrier effects in dispersion models. Follow-on research is underway to complement the current work with a study of upwind barrier and two-barrier configurations.

5. Summary

Two sets of wind tunnel experiments were performed to study the effects of noise barriers downwind of a roadway on traffic-related pollutant concentrations. The *Barrier Height* cases were designed to study the effect of the height of a noise barrier (from 3 m to 9 m) on the plume spread and concentrations downwind of the barrier. The *Source-to-Barrier Distance* cases examined the effect of the distance between a line source and a noise barrier (from 6 m

to 30 m) on downwind concentrations. These cases are useful in examining scenarios where there are lanes of traffic at different distances upwind of a roadside barrier, with each lane acting as an independent line source.

In addition, a mixed-wake algorithm has been further developed (beyond the description provided in Venkatram et al., 2021) based on the noise barrier scenarios modeled in the new wind tunnel studies. This algorithm was designed to reflect three features observed when a plume travels over a solid barrier originating from a roadway: 1) lofting of the main part of the plume to a height just above the top of the barrier, 2) a region of uniform concentration vertically in the well-mixed recirculation region downwind of the barrier, and 3) an enhanced growth rate of the plume due to the turbulence generated in the shear layer above the recirculation zone. Specific changes to the algorithm made in response to the wind tunnel measurements presented in this paper include lofting the plume a height 1.25 times the height of the barrier and reducing the wind speed for the part of the plume in the recirculation region to reflect the lower wind speed immediately downwind of the barrier.

The mixed-wake algorithm was implemented into AERMOD v. 21112 as a non-regulatory option and used to simulate the two sets of wind tunnel experiments. For the most part, the algorithm reproduced the shape of the vertical concentration profiles observed in the wind tunnel data, including the uniform concentration profile from the ground vertically to a height somewhat greater than the height of the barrier. Above this height, the predicted concentrations generally decreased with increasing height following the trend in the wind tunnel measurements, although it did not always capture the slight increase in concentrations above and just downwind of the barrier. The algorithm did respond appropriately to changes in barrier height and source-to-barrier distance, producing greater reductions in ground-level concentrations for taller barriers and for shorter source-to-barrier distances. The model performance was reasonably good, especially for heights less than 6 m, where all model estimates were within a factor of two of the observations and geometric means were below 1.2.

Finally, a rule of thumb that approximates the effect of a downwind barrier was formulated by converting an estimated vertical dispersion into an additional travel distance. The initial vertical dispersion was assumed to be equal to the height of the barrier, h_b, and a further assumption was made that atmospheric stability effects could be ignored in the near-barrier region where mechanically generated turbulence dominates. The resulting rule of thumb states that the effect of the barrier is equivalent to adding an additional travel distance for the plume equal to $x_0 = \frac{h_b}{u_*/U_{hb}}$.

The experiments and model algorithm reported here focused on noise barriers downwind of a roadway. As far as we are aware, these wind tunnel studies are the first experimental results on the effects of barrier height and source-to-barrier distance for barriers downwind of a roadway. Barrier height and source-to-barrier distance both have an impact on downwind concentrations, and these effects diminish for distances farther downwind from the barrier.

Supplementary Material

Refer to Web version on PubMed Central for supplementary material.

8.: Appendix

Model description and setup

The latest release of AERMOD (version 21112) was used to simulate the cases described in section 2.1, the RLINEXT source option with RBARRIER keyword was used in the AERMOD input. The RLINEXT source option is currently a non-regulatory option within AERMOD. The same surface meteorology and profile input files were used for all cases and were developed from the wind tunnel velocity profiles. Because the wind tunnel experiments are steady-state simulations, AERMOD was set up to model the neutrally buoyant atmospheric boundary layer with one hour of meteorological conditions (a reference wind speed of 2.65 m/s at a reference height of 18 m, Obukhov length of 1800, roughness length of 0.27 m, and a friction velocity value of 0.25 m/s). The domain for the calculations extended 222 m downwind from the roadway source and vertically to a height of 36 m above ground level. Concentrations were simulated at heights from $z/H = 0$ to $z/H = 6$ (with a vertical spacing of 0.75 m), and at nine locations along x (at $y = 0$). The vertical profiles were modeled downwind of the barrier at $x/H = 0.125$, 1, 2, 4, 7, 12, 17, 27, and 37.

Road width of 1 m was used for all cases to represent the wind tunnel line source. The line sources were sufficiently long so that there were no edge effects. AERMOD model inputs were tuned to match the wind tunnel results by testing a small range of reasonable initial vertical dispersion coefficient (σ_{z0}) and original source height (z_{src}) values to determine the best *No Barrier* case results. A σ_{z0} of 0.5 m was used for all cases. The z_{src} differed between *Source-to-Barrier Distance* cases (1.85 m) and *Barrier Height* cases (1.5 m). This 0.35-m difference between release heights is equal to a 2.33-mm difference inside the wind tunnel, which could occur from slight differences with the setup of the experiments when changing from the *Source-to-Barrier Distance* cases to *Barrier Height* cases (e.g., deflection of source release bars). Because Q/L_y is the emission rate per unit length (1 g/m/s), the line source emission rate was set at 1 g/m/s for *Source-to-Barrier Distance* cases and 0.5 g/m/s for each line source in the *Barrier Height* cases.

7. References

Ahangar FE, Heist DK, Perry S, Venkatram A, 2017. Reduction of air pollution levels downwind of a road with an upwind noise barrier. Atmos. Environ 155, 1–10. doi: 10.1016/j.atmosenv.2017.02.001

Amini S, Ahangar FE, Heist DK, Perry SG, Venkatram A, 2018. Modeling dispersion of emissions from depressed roadways. Atmos. Environ 186, 189–197. doi: 10.1016/j.atmosenv.2018.04.058

Cimorelli AJ, Perry SG, Venkatram A, Weil JC, Paine RJ, Wilson RB, Lee RF, Peters WD, Brode RW, 2005. AERMOD: a dispersion model for industrial source applications. Part I: general model formulation and boundary layer characterization. J. Appl. Meteorol 44, 682–693. doi: 10.1175/JAM2227.1

Federal Highway Administration (FHWA), 2021. U.S. Department of Transportation. Available online at: https://www.fhwa.dot.gov/environment/noise/noise_barriers/inventory/ (accessed 10 January 2022).

Finn D, Clawson KL, Carter RG, Rich JD, Eckman RM, Perry SG, Isakov V, Heist DK, 2010. Tracer studies to characterize the effects of roadside noise barriers on near-road pollutant dispersion under varying atmospheric stability conditions. Atmos. Environ 44, 204–214. doi: 10.1016/j.atmosenv.2009.10.012

Gromke C, Ruck B, 2012. Pollutant Concentrations in Street Canyons of Different Aspect Ratio with Avenues of Trees for Various Wind Directions. Boundary-Layer Meteorology. 114, 41–64. doi: 10.1007/s10546-012-9703-z

Hagler GSW, Tang W, Freeman MJ, Heist DK, Perry SG, Vette AF, 2011. Model evaluation of roadside barrier impact on near-road air pollution. Atmos. Environ 45, 2522–2530. doi: 10.1016/j.atmosenv.2011.02.030

Han B, Zhao R, Zhang N, Xu J, Zhang L, Yang W, Geng C, Wang X, Bai Z, Vedal S, 2021. Acute cardiovascular effects of traffic-related air pollution (TRAP) exposure in healthy adults: A randomized, blinded, crossover intervention study. Environ. Pollut 288, 117583. doi: 10.1016/j.envpol.2021.117583 [PubMed: 34243086]

Hao C, Xie X, Huang Y, Huang Z 2019. Study on influence of viaduct and noise barriers on the particulate matter dispersion in street canyons by CFD modeling. Atmos. Pollut. Res 10, 1723–1735, doi: 10.1016/j.apr.2019.07.003

Health Effects Institute (HEI), 2010. Traffic-Related Air Pollution: A Critical Review of the Literature on Emissions, Exposure, and Health Effects. HEI Special Report 17, Health Effects Institute, Boston, MA.

Heist DK, Perry SG, Brixey LA, 2009. A wind tunnel study of the effect of roadway configurations on the dispersion of traffic-related pollution. Atmos. Environ 43, 5101–5111. doi: 10.1016/j.atmosenv.2009.06.034

Heist DK, Perry SG, 2018. Wind Tunnels and Dispersion Models. Environmental Managers, Oct. 2018, pp. 13–16.

Irwin HPAH, 1981. The design of spires for wind simulation. J. Wind Eng. Ind. Aerodyn 7, 361–366. doi: 10.1016/0167-6105(81)90058-1

Jerrett M, Finkelstein MM, Brook JR, Arain MA, Kanaroglou P, Stieb DM, Gilbert NL, Verma D, Finkelstein N, Chapman KR, Sears MR, 2009. A cohort study of traffic-related air pollution and mortality in Toronto, Ontario, Canada. Environ. Health Perspect 117, 772–777. doi: 10.1289/ehp.11533 [PubMed: 19479020]

Joerger VM, Pryor SC, 2018. Ultrafine particle number concentrations and size distributions around an elevated highway viaduct. Atmos. Pollut. Res 9, 228–234, doi: 10.1016/j.apr.2018.01.008

Perry SG, Cimorelli AJ, Paine RJ, Brode RW, Weil JC, Venkatram A, Wilson RB, Lee RF, Peters WD, 2005. AERMOD: a dispersion model for industrial source applications. Part II: model performance against 17 field study databases. J. Appl. Meteorol. Climatol 44, 694–708. doi: 10.1175/JAM2228.1

Perry SG, Heist DK, Brouwer LH, Monbureau EM, Brixey LA, 2016. Characterization of pollutant dispersion near elongated buildings based on wind tunnel simulations. Atmos. Environ 142, 286–295. doi: 10.1016/j.atmosenv.2016.07.052

Schulte N, Snyder M, Isakov V, Heist D, Venkatram A, 2014. Effects of solid barriers on dispersion of roadway emissions. Atmos. Environ 97, 286–295.

Snyder MG, Venkatram A, Heist DK, Perry SG, Petersen WB, Isakov V, 2013. RLINE: a line source dispersion model for near-surface releases. Atmos. Environ 77, 748–756.

Snyder WH, 1979. The EPA Meteorological Wind Tunnel: Its Design, Construction, and Operating Characteristics. Report No. EPA-600/4-79-051. U.S. Environmental Protection Agency, Research Triangle Park, NC.

Snyder WH, 1981. Guideline for Fluid Modeling of Atmospheric Diffusion. Report No. EPA-600/8-81-009. U.S. Environmental Protection Agency, Research Triangle Park, NC.

United States Environmental Protection Agency (U.S. EPA), 2021. User's Guide for the AMS/EPA Regulatory Model (AERMOD). Report No. EPA-454/B-21-001. U.S. Environmental Protection Agency, Office of Air Quality Planning and Standards, Research Triangle Park, NC. Available online at: https://www.epa.gov/scram/air-quality-dispersion-modeling-preferred-and-recommended-models#aermod

Venkatram A, 2008. Computing and displaying model performance statistics. Atmos. Environ 42, 6862–6868. doi: 10.1016/j.atmosenv.2008.04.043

Venkatram A, Snyder MG, Heist DK, Perry SG, Petersen WB, Isakov V, 2013. Re-formulation of plume spread for near-surface dispersion. Atmos. Environ 77, 846–855. doi: 10.1016/j.atmosenv.2013.05.073

Venkatram A, Schulte N, 2018. Urban Transportation and Air Pollution. Elsevier, New York, pp. 89 and 145.

Venkatram A, Heist DK, Perry SG, Brouwer L, 2021. Dispersion at the edges of near road noise barriers. Atmos. Pollut. Res 12, 367–374. doi: 10.1016/j.apr.2020.11.017 [PubMed: 33746529]

Wang S, Wang X, 2021. Modeling and analysis of highway emission dispersion due to noise barrier and automobile wake effects. Atmos. Pollut. Res 12, 67–75. doi: 10.1016/j.apr.2020.08.013

Yang H, Chen T, Lin Y, Buccolieri R, Mattsson M, Zhang M, Hang J, Wang Q, 2020. Integrated impacts of tree planting and street aspect ratios on CO dispersion and personal exposure in full-scale street canyons. Build. Environ 169, 106529. doi: 10.1016/j.buildenv.2019.106529

Zhang K, Chen G, Wang X, Liu S, Mak CM, Fan Y, Hang J, 2019. Numerical evaluations of urban design technique to reduce vehicular personal intake fraction in deep street canyons. Sci. Total Environ, 653, 968–994. doi: 10.1016/j.scitotenv.2018.10.333 [PubMed: 30759622]

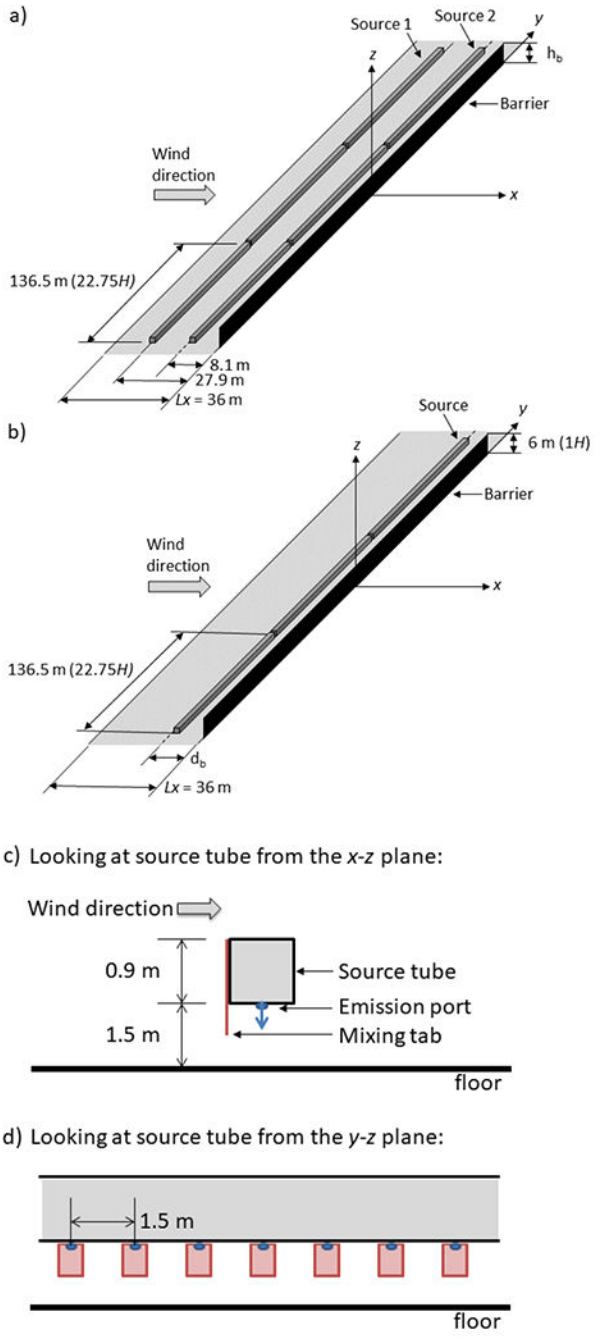

Fig. 1.

Wind tunnel setup with full scale dimensions showing wind flowing along the *x*-axis while the line source(s) and barrier are perpendicular to the *x*-axis. The barrier, when present, was located at $x = 0$ m. a) The *Barrier Height* cases consisted of two fixed line sources and a solid barrier downwind of the sources. The barrier height (h_b) was variable. b) The *Source-to-Barrier Distance* cases consisted of one line source and a solid 6-m-tall barrier downwind of the source. The line source was movable (upwind), which allowed for the study of the source-to-barrier distance (d_b). c) View of source tube (gray bar) showing

emission port (blue dot) at the bottom center of the tube and a mixing tab (red) on the upwind face of the tube. d) View of source tube segment (looking upwind) to show the spacing between emission ports.

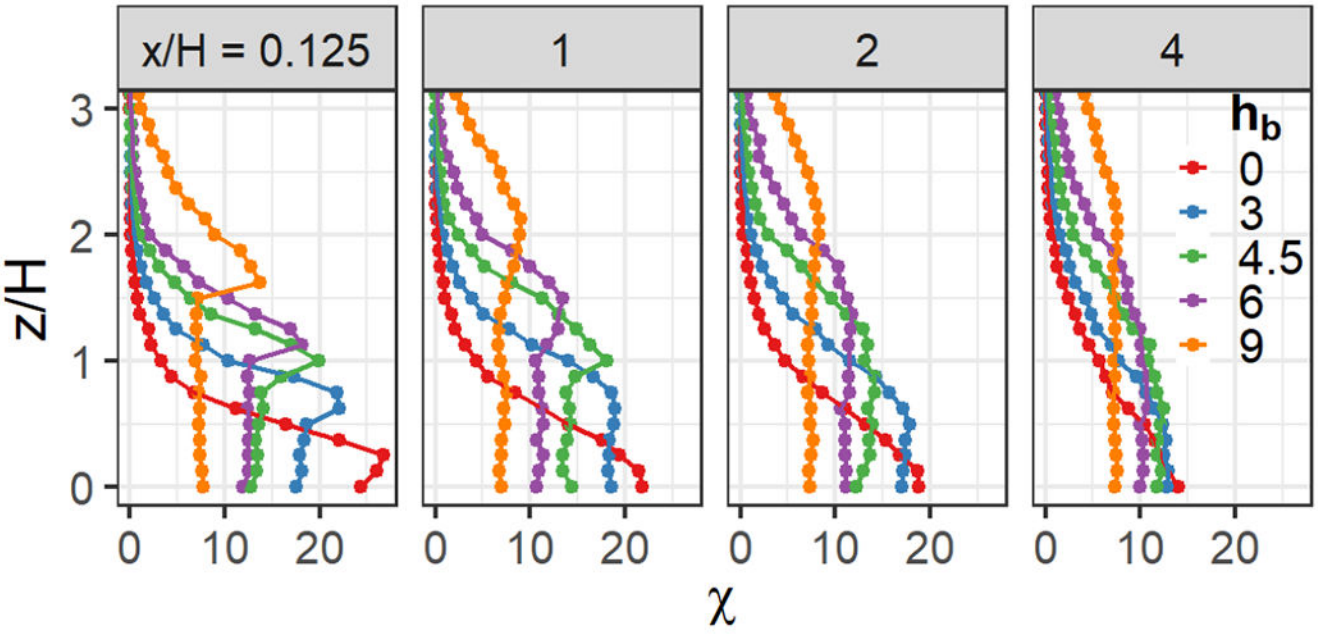

Fig. 2.

Vertical profiles of normalized concentrations (χ) as a function of normalized height (z/H) for the *Barrier Height* cases, including the *No Barrier* case (0 m) and *Barrier* cases of various barrier heights (3–9 m). Each panel shows a downwind distance from the barrier (x/H). The barrier, when present, is located at $x/H = 0$. Dots depict the measured concentrations in the wind tunnel, and the connecting line highlights vertical plume shape. Note: $H = 6$ m regardless of barrier height.

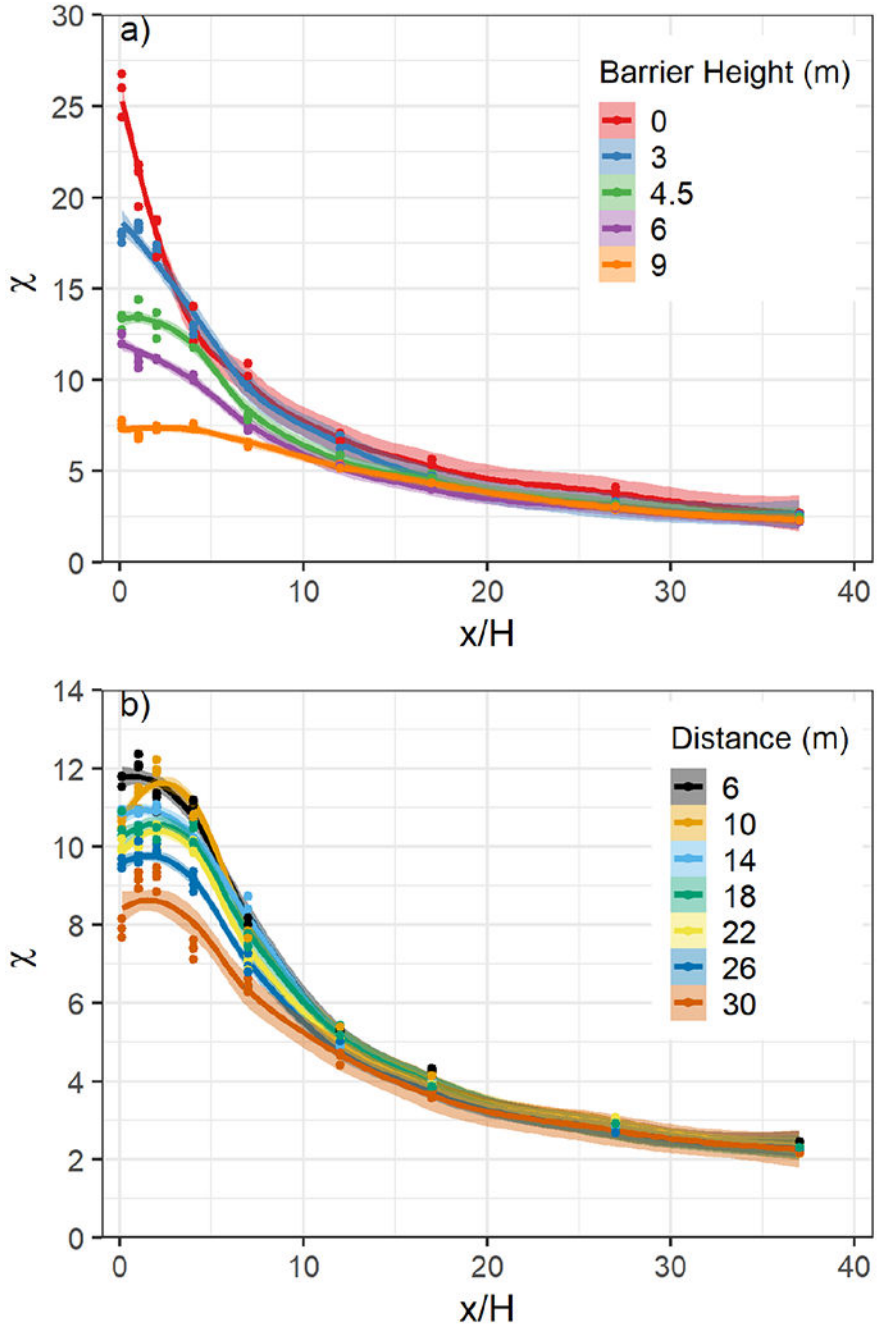

Fig. 3.

Normalized concentration (χ) vs. downwind distance from the barrier (x/H) within the breathing level ($z/H = 0$ to $z/H = 0.33$) for a range of barrier heights (m). The barrier, when present, is located at $x/H = 0$. Dots depict the measured concentrations in the wind tunnel and the shading of the smoothed lines represents the spread of the wind tunnel measurements within the breathing level using a locally estimated scatterplot smoothing (LOESS) method with span of 0.6. The shading around the line shows a 95% confidence

interval. Note: H = 6 m regardless of barrier height. a) *Barrier Height* cases. b) *Source-to-Barrier Distance* cases. The barrier has a height of 6 m. The *No Barrier* cases are not shown.

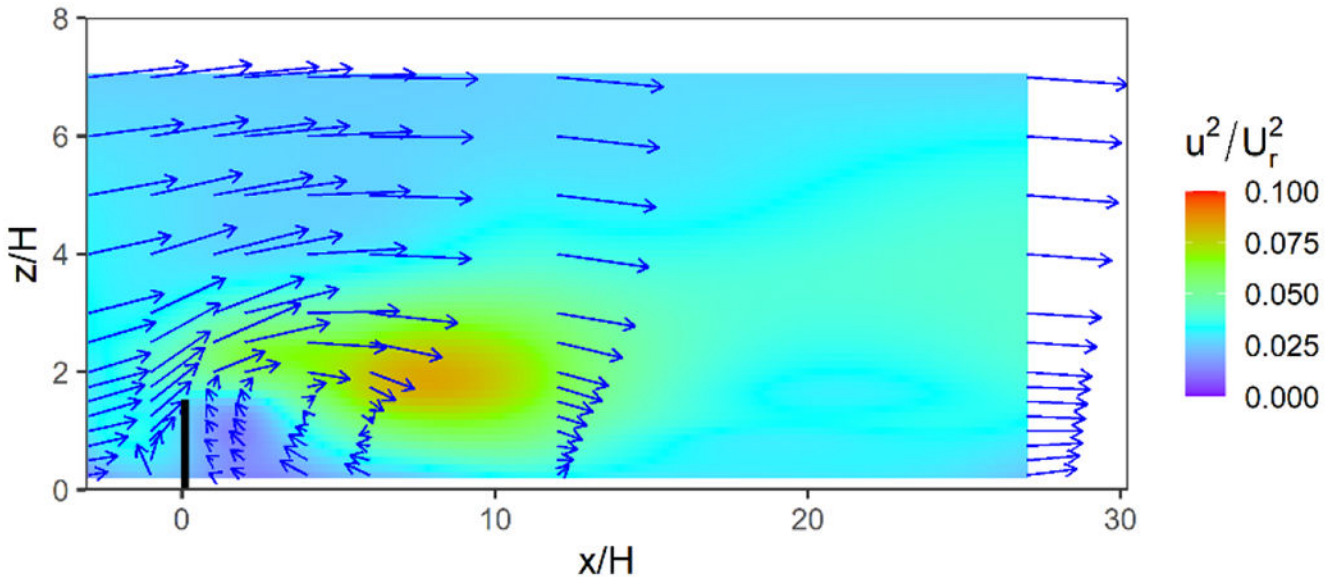

Fig. 4.

Mean velocity vectors as a function of normalized height (*z/H*) vs. downwind distance for the tallest *Barrier* case. The barrier is located at $x/H = 0$ and has a height of 9 m. The blue arrows indicate mean wind vectors, which show the flow surrounding the barrier (black bar). Shaded contours represent the x-axis component of turbulence $\left(u^2/U_r^2\right)$. Wind velocity and turbulence measurements from the wind tunnel are located at $x/H = -3, -1, 1, 2, 4, 6, 12,$ and 27.

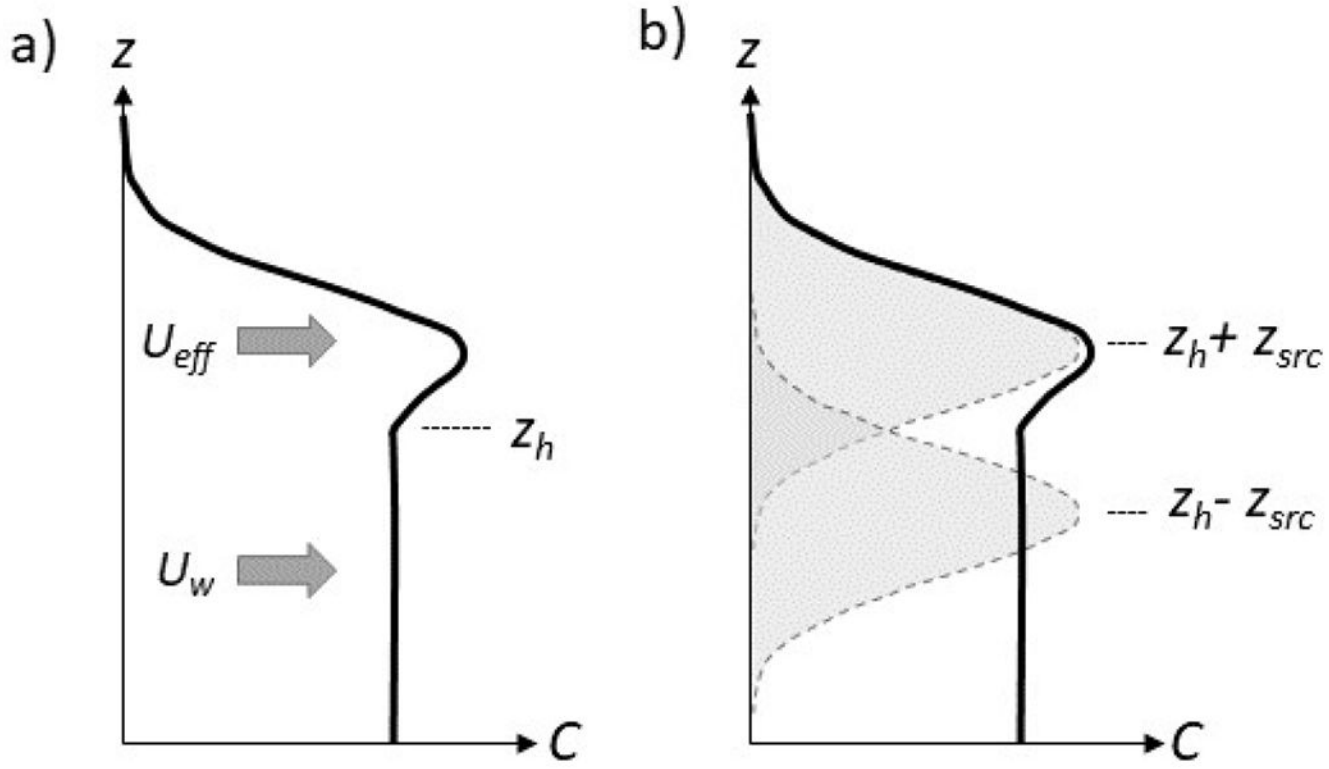

Fig. 5.

Idealized schematic diagram of a vertical concentration profile immediately downwind of a downwind barrier showing the structure of the mixed-wake concept. a) The concentration is uniform from the ground to a height z_h, above which it initially rises to a peak before falling off with height. U_{eff} is the advection velocity for the upper portion of the plume and U_w is the advection velocity for the lower portion of the plume. b) The upper portion of the profile, above z_h, is modeled with a source at $z_h + z_{src}$ (and a reflected source at $z_h - z_{src}$).

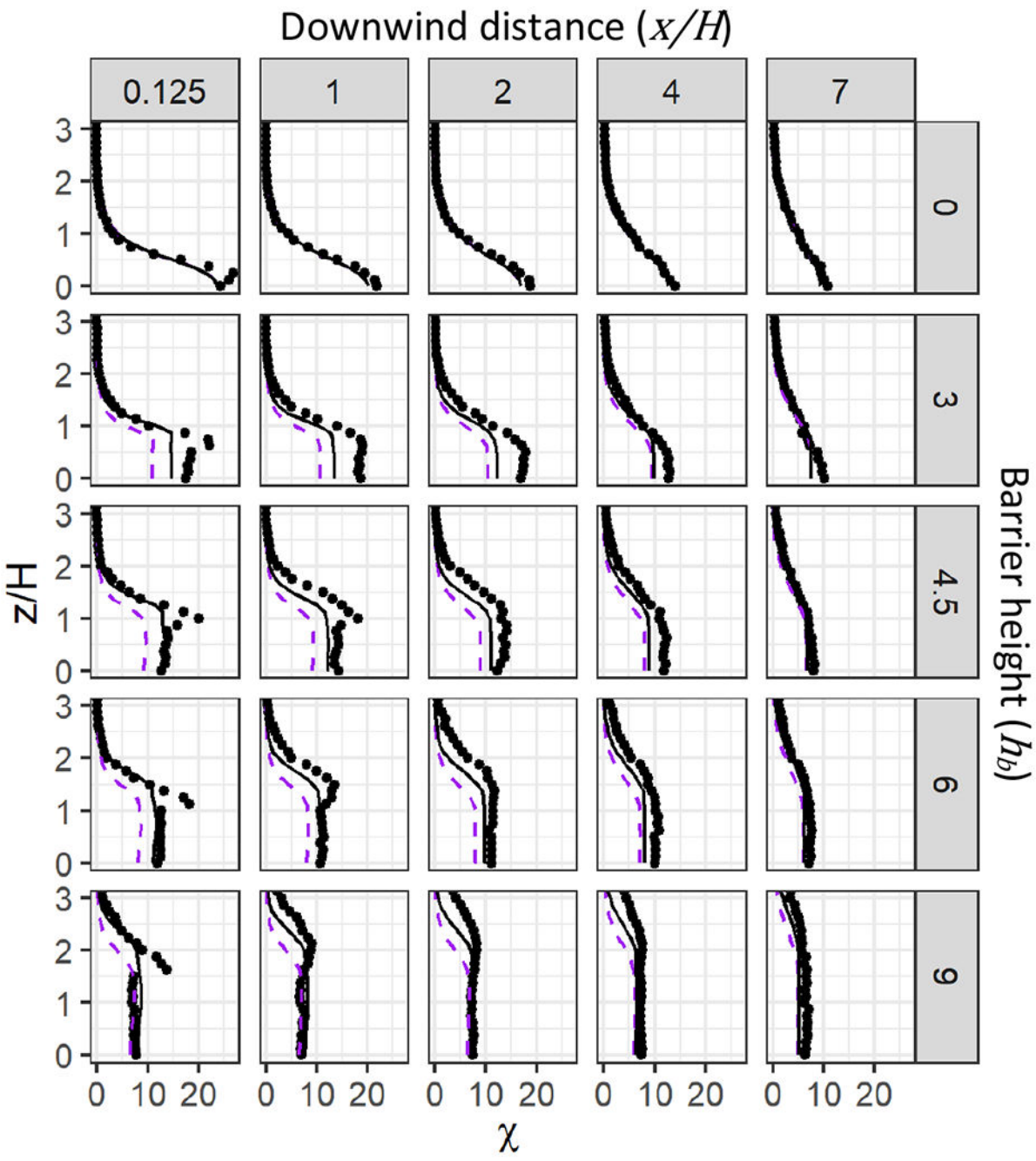

Fig. 6.

Vertical profiles of normalized concentrations (χ) for the *No Barrier* case (0 m) and *Barrier* cases at various barrier heights (3–9 m). Each column shows downwind distance from the barrier (*x/H*). The barrier, when present, is located at $x/H = 0$. Each row shows cases labeled as barrier height (m). Black dots represent wind tunnel measurements, black solid lines represent AERMOD model results, and purple dashed lines represent the previous version of the barrier algorithm (see text for details). Note: $H = 6$ m regardless of barrier height.

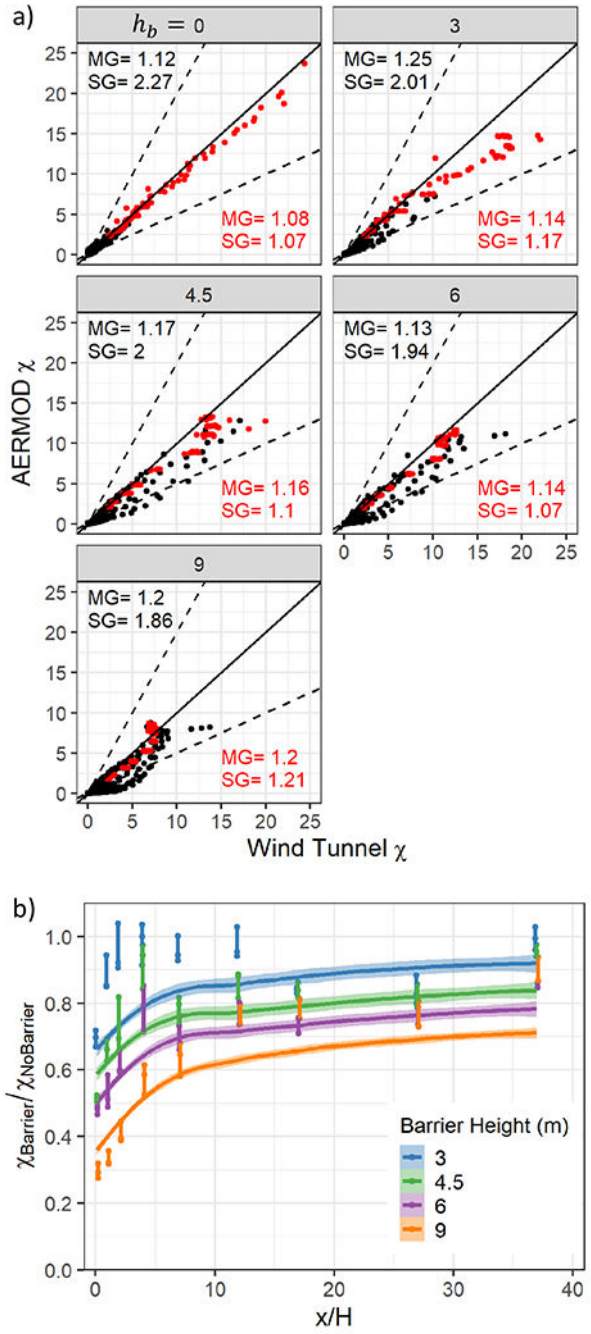

Fig. 7.

a) Normalized concentration (χ) comparison between AERMOD results and wind tunnel measurements. Each panel plot is a case labeled with barrier height (m). *No Barrier* case (0 m) and *Barrier* cases with barrier heights of 3 m, 4.5 m, 6 m, and 9 m are shown. Concentration values in red are a subset of the data at sample locations from ground level (0 m) to 6 m. Dashed lines represent the factor of two for concentration values. Each panel plot (case) shows geometric mean (MG) and geometric standard deviation (SG) statistics for all sample locations (black) and the ground level to 6-m elevations (red). b) Normalized

concentration ratios ($\chi_{Barrier}/\chi_{NoBarrier}$) vs. downwind distance from the barrier (x/H) within the breathing level ($z/H = 0$ to $z/H = 0.33$) for a range of barrier heights (3–9 m). The barrier is located at $x/H = 0$. Wind tunnel measurements (dots) and AERMOD model results (lines) are shown for the breathing level. The model result lines use a locally estimated scatterplot smoothing (LOESS) method with span of 0.75. Wind tunnel measurements in the breathing level are connected with a vertical line at each x/H location, which is then displaced slightly to avoid overlapping other cases. The shading around the line shows a 95% confidence interval.

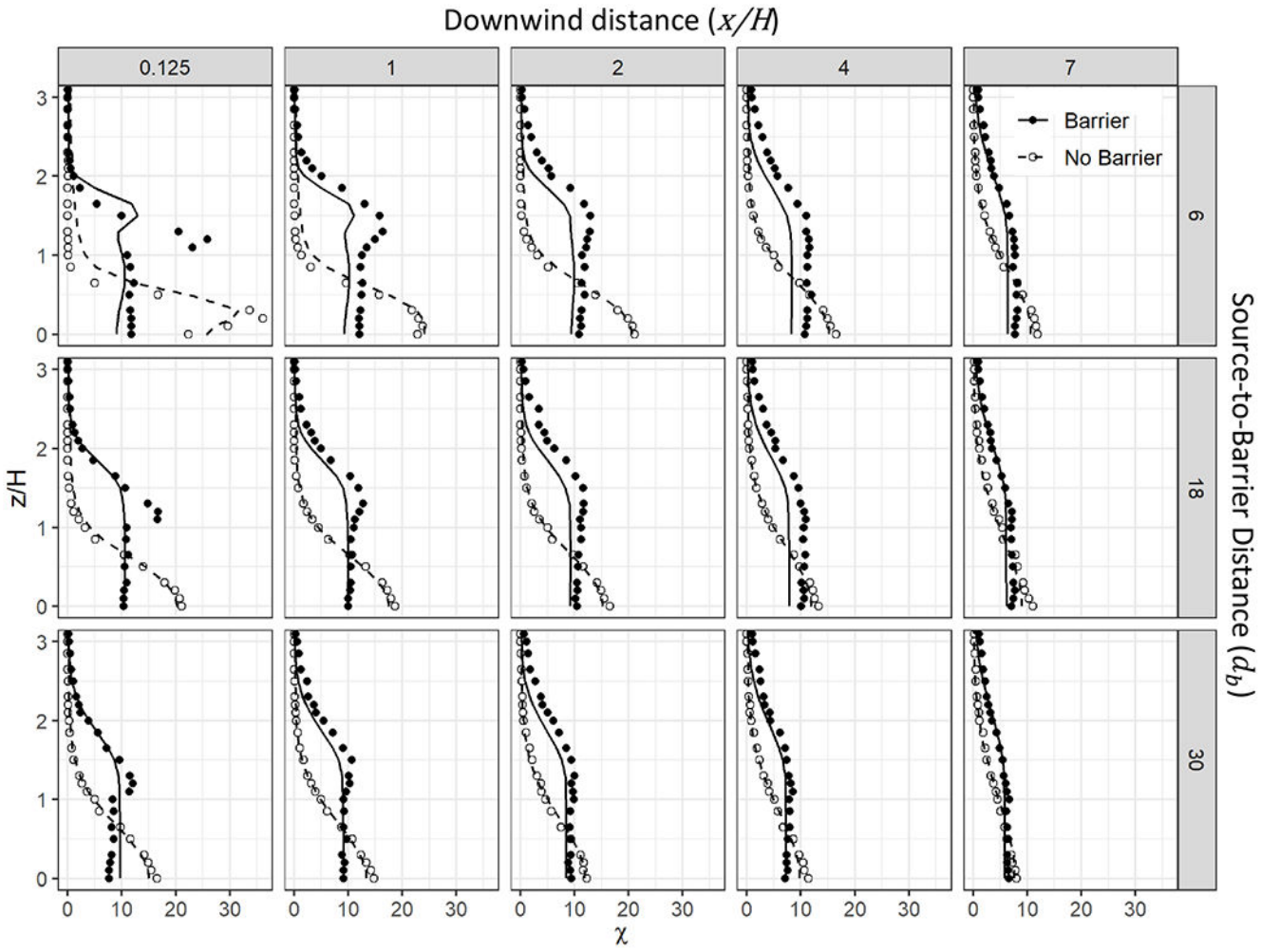

Fig. 8.

Vertical profiles of normalized concentrations (χ) for the *No Barrier* case and *Barrier* cases at various source-to-barrier distances (6–30 m). Each column shows downwind distance from the barrier (x/H). The barrier, when present, is located at $x/H = 0$. Each row shows cases labeled as source-to-barrier distance (m). Dots represent wind tunnel measurements and solid lines represent AERMOD model results. *Barrier* cases (solid dot and line) shown are for source-to-barrier distance of 6 m, 18 m, and 30 m. *No Barrier* cases (open dot and dashed line) are shown at the same locations for comparison.

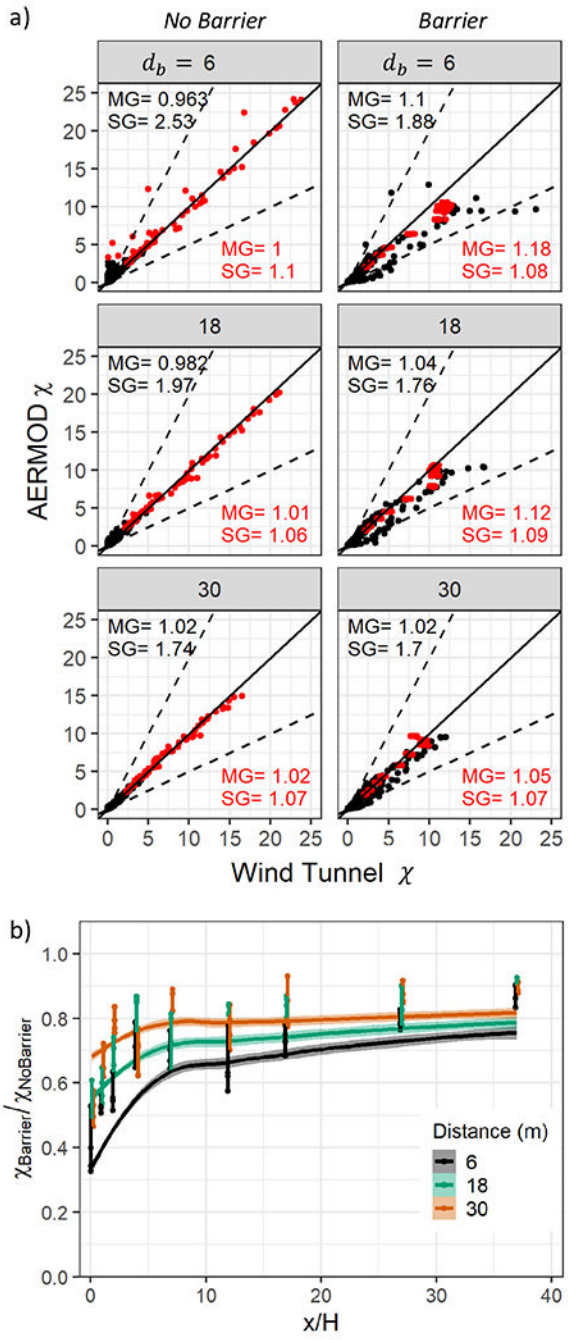

Fig. 9.

a) Normalized concentration (χ) comparison between AERMOD results and wind tunnel measurements. Each panel plot is a case labeled with the source-to-barrier distance (m). *Barrier* cases are shown in the right column for source-to-barrier distances of 6 m, 18 m, and 30 m. The *No Barrier* cases for the same distances are shown in the left column. Concentration values in red are a subset of the data at sample locations from ground level (0 m) to the barrier height (6 m). Dashed lines represent the factor of two for concentration values. Each panel plot (case) shows geometric mean (MG) and geometric

standard deviation (SG) statistics for all sample locations (black) and ground level to barrier height elevations (red). b) Normalized concentration ratios ($\chi_{Barrier}/\chi_{NoBarrier}$) vs. downwind distance from the barrier (x/H) within the breathing level ($z/H = 0$ to $z/H = 0.33$) for a range of source-to-barrier distances (6–30 m). The barrier is located at $x/H = 0$. Wind tunnel measurements (dots) and AERMOD model results (lines) are shown for the breathing level. The model result lines use a locally estimated scatterplot smoothing (LOESS) method with span of 0.75. Wind tunnel measurements in the breathing level are connected with a vertical line at each x/H location, which is then displaced slightly to avoid overlapping other cases. The shading around the line shows a 95% confidence interval.

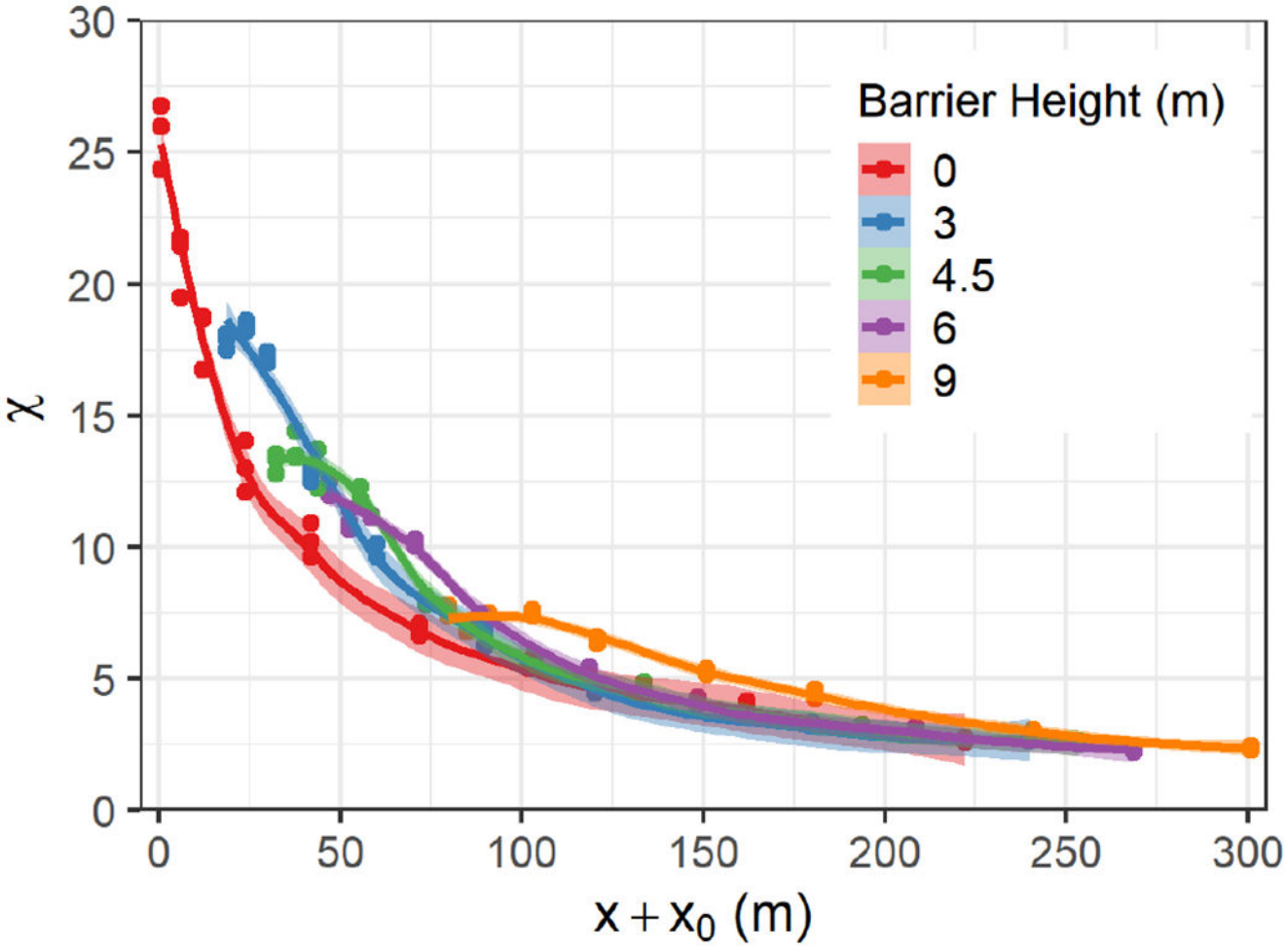

Fig. 10.

Normalized concentration (χ) vs. a shifted downwind distance ($x + x_0$) from the barrier within the breathing level ($z/H = 0$ to $z/H = 0.33$) for a range of barrier heights. *Barrier* cases were shifted downwind by an additional travel distance, x_0 (m). The barrier, when present, is located at $x/H = 0$. Dots depict the measured concentrations in the wind tunnel and the smoothed lines with shading represent the spread of the wind tunnel measurements within the breathing level using a locally estimated scatterplot smoothing (LOESS) method with span of 0.6. The shading around the line shows a 95% confidence interval.